Proceedings of the 21st ICSMGE, Vienna, Austria, 14 – 19 June 2026. Pistrol, Adam & Schweiger (eds.)
Published by: ÖGG, Austrian Society for Geomechanics, Salzburg, Austria, ISBN 978-3-9503898-4-5
https://doi.org/10.53243/ICSMGE2026-1482

Multiscale Assessment of the Interface Shear Behavior Between Snakeskin-Inspired Surfaces and Coarse-Grained Soils

Damon Nguyen, **Alejandro Martinez**
Civil and Environmental Engineering, University of California, Davis, USA, dtlnguyen@ucdavis.edu

ABSTRACT: The performance of many geotechnical structures relies on sufficient resistance mobilized at soil-structure interfaces. These systems may benefit from surface textures that mobilize frictional directionality, where greater strength is developed in one direction as opposed to the other. To this end, inspiration is drawn from snakes' ventral scales which facilitate smooth forward sliding and increased frictional resistance in the reverse direction. Discrete element modelling (DEM) is used to conduct monotonic interface shear simulations on coarse-grained soil specimens in contact with snakeskin-inspired surfaces to shed light on the load transfer mechanisms that arise in both shearing directions. Significantly larger shear resistances are mobilized when shearing occurs against asperities (i.e. cranially) than along asperities (i.e. caudally). Interface strength increases with increasing asperity height and decreasing asperity length, in agreement with experimental trends. Particle level analysis shows that during cranial shear, the edges of asperities interlock with neighboring particles, causing significant displacements and mobilizing local passive resistances characterized by strong force chains. In addition, frictional resistances are mobilized due to the sliding between particles and asperities. Spacing affects the interaction between individual asperities, and these interactions influence both passive and frictional resistances. During caudal shear, asperities do not produce much particle displacement or mobilize significant passive forces. Instead, slippage between particles and asperities is the primary failure mode, which is less dependent on asperity geometry.

KEYWORDS: Discrete element modeling, bio-inspiration, interface shear.

1 INTRODUCTION

In many geotechnical systems, such as deep foundations and anchorage elements, the mobilization of skin friction is a design consideration of paramount importance. Many systems mobilize similar frictional resistances regardless of load direction, though several applications may benefit from the ability to mobilize directional-dependent friction. Some examples include foundations for solar panels and offshore wind turbines and driven soil anchors. In these cases, resistance to pullout can be enhanced while the skin friction during installation can be reduced, potentially increasing service life and decreasing environmental impacts. To this end, inspiration has been taken from the ventral scales along the underbelly of snakes. The unique geometries of these scales enable snakes to smoothly slide over the substrate and propel themselves with minimal resistance. When pulled backwards, the edges of the scales grip onto the substrate, greatly increasing interface friction and allowing snakes to anchor their bodies (Hu et al. 2009; Jayne, 1986). The surfaces of geotechnical systems can be textured with asperities that mimic ventral snake scales, enabling frictional directionality (Martinez et al. 2022).

Previous investigations on the interface shear behavior of snakeskin-inspired surfaces have shown that it depends on both the shear direction and geometry of the asperities. The shear strength mobilized when shearing in the cranial direction (i.e., against the asperities) is significantly greater than that mobilized in the caudal direction (i.e., along the asperities) (Martinez et al. 2019). Shear strength correlates strongly with both the length (L) and height (H) of asperities. As L decreases or H increases, shear strength increases. (Gayathri et al. 2022; Lee et al. 2023; Xiao et al. 2024; O'Hara and Martinez 2024). The interactions between asperities and sand were explored further with particle image velocimetry, where it was found that cranial shear of surfaces with high L resulted in the mobilization of wedges at each asperity, while other cases produced more uniform deformations (Martinez et al. 2019).

The mechanics behind these observations remain unclear, warranting deeper investigation of particle- and asperity-level interactions during interface shear. Discrete element modelling (DEM) is used here to build upon previous insights and gain a better understanding of how shear resistance is mobilized. Interface shear simulations are performed with snakeskin-inspired surfaces with varying asperity geometries. The results of these simulations are analyzed to observe the mobilization of passive resistances and localized deformation zones. Specifically, this analysis aims to explain the mechanisms leading to frictional directionality and provide insight into how asperity geometry influences shear behavior.

2 SIMULATION METHOD

2.1 *Simulated material*

Monotonic interface shear simulations were performed using PFC 3D version 5.0 (Itasca, Minneapolis, MN) with the linear contact model with rolling resistance. Spring and dashpot components were used to calculate contact forces. Springs with normal and shear stiffnesses (k_N and k_S) provide linear elastic frictional behavior. k_N was equal to the product of the particle diameter (d) and elastic stiffness modulus (E) and k_S was calculated based on a stiffness ratio (k_N/k_S). Dashpots of normal and shear damping ratios (β_N and β_S) provided viscous behavior. A coulomb limit on shear force and a limit to relative rotation were defined by coefficients μ and μ_r, respectively.

Table 1. Contact parameters for simulated Ottawa F65 sand.

Parameter	Symbol	Value	Unit
Interparticle friction	μ	0.51	-
Rolling resistance	μ_r	0.26	-
Stiffness modulus	E	1.00E+08	Pa
Stiffness ratio	k_N/ks	1.50	-
Damping ratios	β_N *and* β_S	0.10	-
Density	ρ	2650	kg/m^3
Wall friction	μ_k	0.20	-
Wall stiffness	$k_{N,k}$	1.42E+07	N/m
Wall stiffness ratio	$k_{N,k}/ks,k$	1.50	-

DEM parameters were calibrated to replicate the behavior of Ottawa F65, a poorly graded, sub-rounded sand with D_{50} = 0.21 mm, C_U = 1.64, and C_C = 1.01. The calibration procedure used drained triaxial test simulations, where contact parameters were initially estimated based on response surfaces and then iterated to match the experimental behavior reported by Blair (2024). Table 1 lists the calibrated parameters, Figure 1a compares stress-strain responses from triaxial simulations and experiments, showing a good match of the peak sand critical

state strengths and initial stiffness for three different relative densities. Nguyen et al. (2025) provide additional details of this calibration procedure. The wall parameters for the interface shear simulations were selected to model an idealized smooth material surface. Figure 1b shows the grain size distribution (GSD) of Ottawa F65 and the simulated material. An unscaled GSD was used for the calibration exercise, while the GSD and specimen size were upscaled by a factor of 20 for interface shear simulations to reduce computational times.

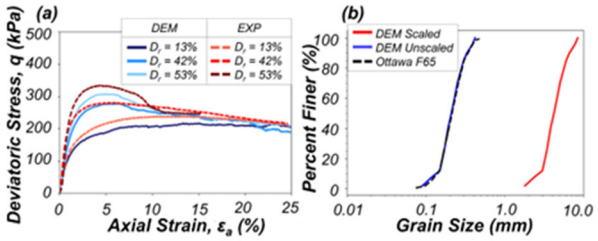

Figure 1. (a) DEM simulated and experimental triaxial compression tests, and (b) GSDs of DEM sand and Ottawa F65 sand.

2.2 *Set-up and procedure*

Simulations were performed on rectangular specimens, as shown in Figure 2a. Rigid top and bottom boundaries were used, while the four lateral sides modeled periodic boundaries, simulating an infinite plane. The top surface was comprised of evenly spaced plates that applied a constant normal stress using a servo-control algorithm. Vertical shear keys were employed at the top of the specimen to engage the soil and ensure that deformations occur at the bottom of the specimen. The spacing of the shear keys was reduced until its effect on the shear behavior was negligible. Before shearing, the shear keys extend about $3D_{50}$ into the specimen. This depth was determined to be sufficient to engage the soil through a sensitivity study. The shear keys are sufficiently tall to accommodate the upward displacement of the top plates due to soil dilation, which varied based on the geometry of the asperities. However, their full height is not shown in the figures for clarity.

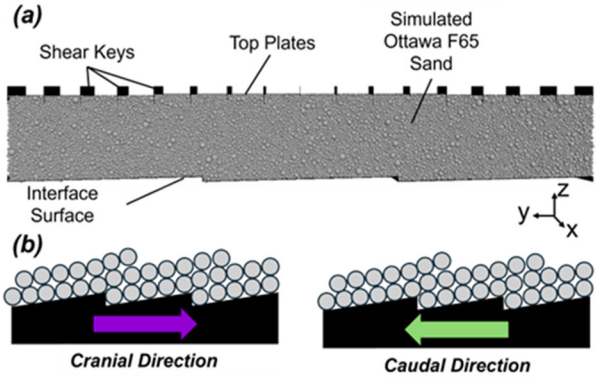

Figure 2. (a) Specimen for interface shear simulations and (b) schematics of shearing in the cranial and caudal directions.

The bottom shear surface, whose geometry varies by case, was displaced horizontally in the y direction during shear. The smooth reference surface consisted of a flat surface with no asperities. The rough reference surface was constructed with a sawtooth pattern with a tooth length of $6.2D_{50}$ and tooth height of $2.4D_{50}$. The nine snakeskin inspired surfaces consisted of straight-lined, right-triangular asperity shapes inspired after the scales of a western hognose snake (Martinez et al. 2019). The asperity height (H) was varied between simulations between values of $0.5D_{50}$ to $1.4D_{50}$ while the length (L) was varied between $29D_{50}$ and $86D_{50}$. Snakeskin-inspired surfaces were sheared in both cranial and caudal directions, as illustrated in Figure 2b. Specimen dimensions were determined through a size sensitivity study were incremental increases were made to each dimension until further changes did not affect the interface shear behavior. After this process, a width of $14D_{50}$, length of $171D_{50}$, and height of $25D_{50}$ (from shear surface to shear key bottom) were chosen, resulting in specimens of about 127,000 particles.

The interface shear simulations included three phases. In the first phase, an initial state is created where particles are randomly placed in the specimen, forming a cloud of particles. The system is then cycled to resolve overlaps and forces. Next, during compression, the top plates impose a constant normal stress (σ_N) of 80 kPa through servo control. Finally, shearing is performed by quasi-statically displacing the bottom surface laterally until a horizontal displacement (δ_H) of $28.6D_{50}$ is accrued. All simulations were performed on specimens with a void ratio of 0.53. All other parameters besides the geometry of the shear surface were kept constant between simulations.

3 GLOBAL SHEAR BEHAVIOR

Both cranial and caudal shearing direction and asperity geometry influenced interface shear behavior. Figure 3 presents the evolution of the shear stress (τ) and vertical displacement (δ_V) normalized by D_{50} as a function of horizontal displacement (δ_H) normalized by D_{50} for each simulation. In each plot, L is held constant while H and the shear direction are varied. The behaviors of the reference rough and smooth surfaces are shown by the black and grey dashed lines, respectively.

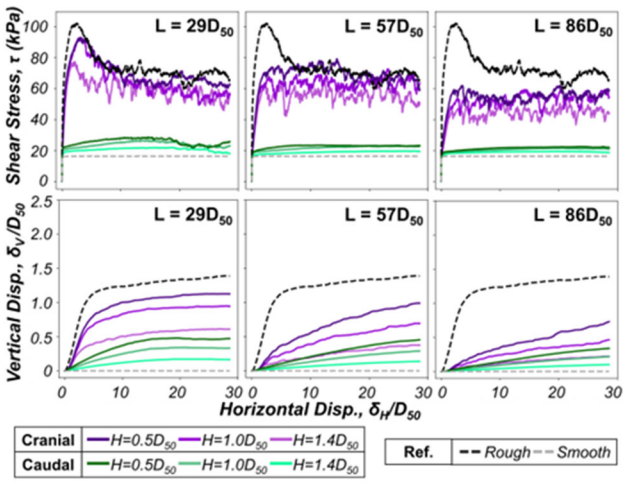

Figure 3. Shear stress and vertical displacement as a function of horizontal displacement for interface shear simulations.

The rough surface mobilized the highest peak τ, strain softening, rate of dilation, and vertical displacements, while the smooth reference surface mobilized the smallest τ with negligible strain softening and volumetric changes. These trends were expected and match experimental observations (e.g., Uesugi and Kishida 1986; Dietz and Lings 2006; Martinez and Frost 2017). Both surfaces produced very similar behaviors regardless of shearing direction; thus, only the results of one direction are presented

Cranially sheared specimens mobilized significantly larger τ and had more dilative behavior than caudally sheared specimens for all geometry types. At the lowest L of $29D_{50}$, cranial shearing mobilized strain-softening behavior similar to that observed for the rough surface. The rough surface mobilized slightly higher shear strength than surfaces with the two tallest H values. For the shortest H value of $0.5D_{50}$, peak τ was lower and strain softening was less pronounced than in the

other cranial cases. At an L of $57D_{50}$, all three H values mobilized strain-hardening behavior, showing less similarity to the response of the rough surface. Still, the residual τ for these cases were similar to the values mobilized for surfaces with an L of $29D_{50}$. Strain-hardening behavior was again observed at an L of $86D_{50}$, accompanied by even lower shear strengths. Generally, as H decreases and L increases, shear behavior diverges from that of the rough surface, with reduced strain softening, lower mobilized shear resistance, and less dilation.

Caudally sheared specimens produced responses that were more similar to that of the smooth surface, but the shear strength and volumetric changes were greater in the caudally sheared specimen. Both shear strength and dilative volume changes increased as H increases. Although increases in L led to reductions in both shear strength and dilation, the effect was generally less pronounced than for cranial shear. Overall, the behavior of caudally sheared specimens was less influenced by asperity geometry than the cranially sheared specimens. These observations highlight key aspects of frictional directionality for snakeskin-inspired surfaces and are in agreement with experimental trends.

4 PARTICLE-LEVEL MECHANISMS

Interface shear response arises from interactions between particles and asperities, which are governed by both asperity geometry and shearing direction. These interactions shape the global shear behavior and were investigated through contact force and particle displacement distributions.

4.1 *Contact force distributions*

Both shear direction and asperity geometry influenced the contact force distributions, as shown in Figure 4 at the end of shearing (i.e., $\delta_H = 29D_{50}$). Shearing of the rough surface mobilized a uniform distribution of strong, diagonal force chains (Figure 4a) in agreement with Wang et al. (2007). Shearing of the smooth surface mobilizes a greater number of primarily vertical, weaker force chains (Figure 4b).

Snakeskin-inspired surfaces produced distinct contact force distributions in each shear direction, unlike the reference surfaces. For cranially sheared snakeskin-inspired surfaces, strong force chains propagated from the front sides of each asperity, creating localized areas of high contact force magnitudes. The surface with asperities of $H = 1.4D_{50}$ and $L = 29D_{50}$ produces six groups of strong force-chain branches, corresponding to the six asperities (Figure 4c). The contact force distribution for this case shares similarities with that of the rough surface, in agreement with the shear-strain behavior (Figure 3). The surface with $H = 1.4D_{50}$ and $L = 57D_{50}$ produces a contact force distribution that was not uniformly distributed across the specimen, with concentrations ahead of the three asperities (Figure 4d). The greater spacing between asperities in comparison to that with an $L = 29D_{50}$ produced force chain groups with larger magnitudes and wider extents across the specimen. While these groups of force chains were stronger, the size of regions between asperities with fewer, weaker contacts also increased. Considering the similar residual interface strength mobilized by the specimens in Figure 4b and Figure 4c (Figure 3), it can be deduced that the load transfer contribution per asperity in the latter surface is greater. The force chain map of a cranially sheared specimen with $H = 0.5D_{50}$ and $L = 57D_{50}$ is presented in Figure 4e, showing weaker, less prominent groups of contact forces mobilized on the front side of each asperity. This maps to a smaller interface shear strength (Figure 3). Generally, when L is sufficiently small, strong forces chains are more uniformly distributed across the specimen in a similar manner to what is mobilized by the rough surface. As L is increased, strong forces become more localized on the front sides of asperities. As H is increased, the surface area of the asperity front side increases, engaging more particles and produces a greater number of strong contact forces.

While the shear strain behaviors mobilized by caudally sheared snakeskin-inspired surfaces and the smooth surfaces were similar (Figure 3), the contact force distributions were distinct from one another. Caudal shear mobilized force chains that concentrate on the advancing sides of asperities. Force chains were propagated vertically upwards with a tilt towards the shearing direction. Unlike cranial shear, the areas behind the asperities' vertical faces showed an absence of force chains. While the smooth surface produced a more homogenous distribution of force chains, caudal shear produced localized areas of greater contact forces at each asperity. This indicates that while the shear strength mobilized by the caudally sheared and smooth surfaces were similar, different particle behaviors occur during shear, as evident by both the contact force distributions and the dilative behaviors. Though not shown in Figure 4, caudal shear produced similar contact force distributions for different asperity geometries. However, shallower slopes of the advancing sides of asperities (i.e., greater L and smaller H) resulted in weaker magnitudes of force chains.

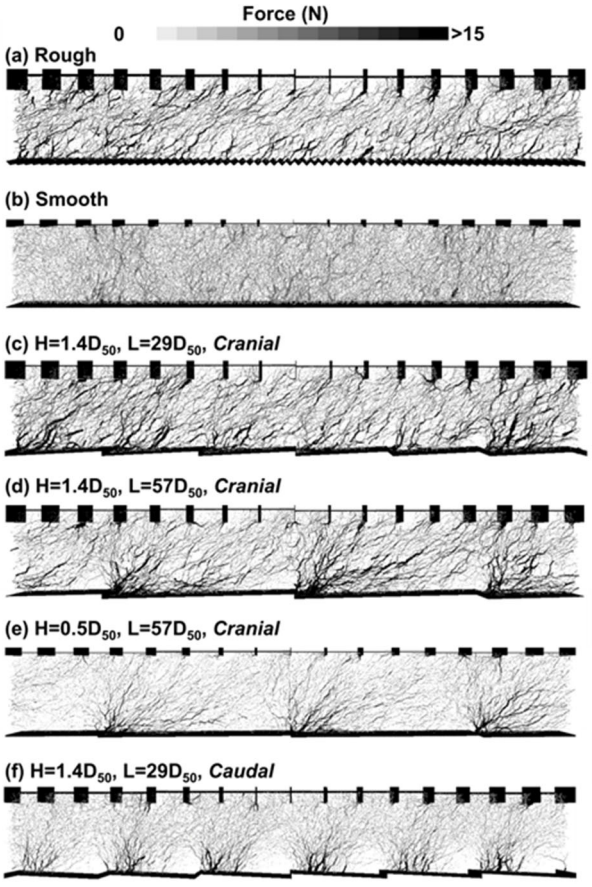

Figure 4. Normal contact forces at the end of shearing ($\delta_H = 29D_{50}$) for select surface geometries.

4.2 *Particle Deformation patterns*

The accumulated particle displacements at the end of shearing are presented in Figure 5 for the same set of simulations shown in Figure 4. A uniform shear band adjacent to the surface was developed by the rough surface (Figure 5a), agreeing with prior studies (e.g., Jing et al. 2018; Zhang and Evans 2018; Zhong et al. 2021). In contrast, little to no particle displacements were

generated by the smooth surface, as the primary interaction between particle-surface contacts was sliding. (Figure 5b).

The snakeskin-inspired surfaces produced different particle deformation patterns depending on the shear direction and asperity geometry. Cranial shear with the surface with H = $1.4D_{50}$ and L = $29D_{50}$ produced deformations localized within a uniform band (Figure 5c) in a similar manner to the simulation with the rough surface. A different deformation pattern was observed from cranial shearing of the surface with H = $1.4D_{50}$ and L = $57D_{50}$, which mobilized wedges with localized displacements at the leading front of the asperities (Figure 5d). These wedges formed as the asperities pushed particles trapped near the corners of the surface, while other particles were able to roll over the edges to the smooth back side of the asperities, where their interactions with the surface were primarily governed by sliding. Comparison of these deformation patterns with those from the surface with the shorter L = $29D_{50}$ (Figure 5c) shows that larger values of L, which represents the spacing between the front of the asperities, allow for passive wedges to develop. In contrast, small L values promote more uniform deformations similar to a fully rough surface. The surface with H = $0.5D_{50}$ and L = $57D_{50}$ also produces individual passive wedges. However, particle displacement magnitudes are significantly smaller due to small H (Figure 5e).

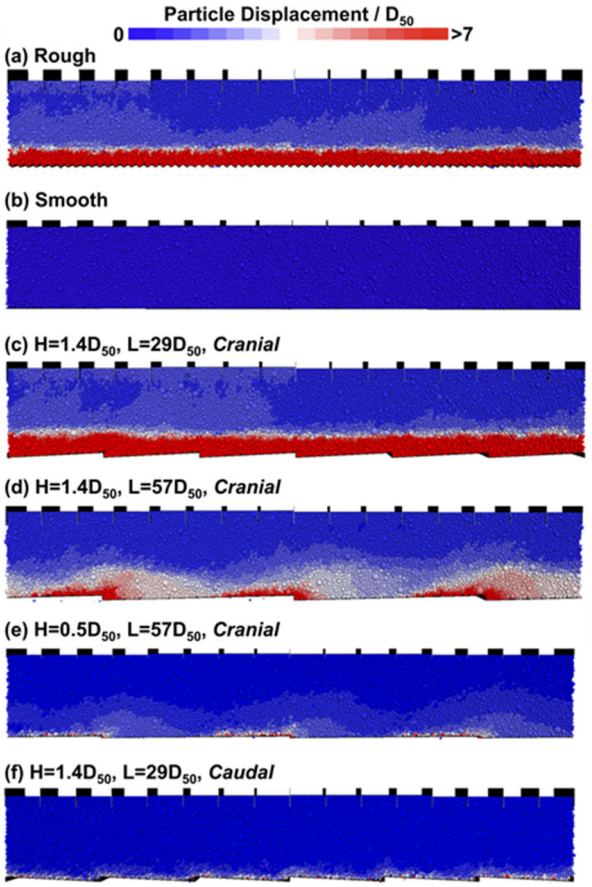

Figure 5. Total particle displacements at the end of shearing (δ_H = $29D_{50}$) for select surface geometries.

The particle displacements resulting from caudal shearing were significantly smaller than those resulting from cranial shearing, but greater than those from shearing of the smooth surface. It is inferred that the load at the interface is being transferred by sliding in a similar manner to the smooth surface. However, instead of sliding along a flat surface, particles travelled upwards along the sloped sides of the asperities, mobilizing new interparticle contacts, and resulting in greater dilation. For the surface with the greatest asperity slopes (H = $1.4D_{50}$, L = $29D_{50}$), caudal shearing resulted in some particle deformations at the surface (Figure 5f). While not shown in Figure 5, caudal shearing of surfaces with shallower asperity slopes resulted in less particle displacements and more closely resembled the behavior of the smooth surface.

The trends in particle displacements are in agreement to those observed for the global shear behavior (Figure 3) and contact force distributions (Figure 4). Cranial shear produced similar responses to the fully rough surfaces when H is large and L is small. As L was increased, the behavior transitioned to becoming more passive dominant, where localized areas of stress and deformation dictated shear resistance. The behavior of caudally sheared specimens shared similarities to the behavior from the smooth surface. However, caudally sheared surfaces resulted in contact force distributions comprised of groups of force chains that induced greater particle displacement with steeper asperity slopes.

5 FORCE COMPONENTS IN LOAD TRANSFER

The mobilized interface shear resistance of the snakeskin-inspired surfaces is comprised of three force components acting on the asperities, as illustrated in Figure 6. The passive component (F_P) acts perpendicular to the vertical side of the asperity in the y-direction, the normal force component (F_N) acts perpendicular to the smooth surface of the asperities, and the frictional sliding component (F_S) acts parallel to surface. Shearing is performed along the y-direction. Therefore, the F_N and F_S are resolved into y-components ($F_{N\text{-}Y}$ and $F_{S\text{-}Y}$, respectively) to quantify their contributions to shear resistance. The y-components of F_N and F_S are calculated from Equation (1) and Equation (2) as follows:

$$F_{N-Y} = F_N \times sin(\theta) \quad (1)$$

$$F_{S-Y} = F_S \times cos(\theta) \quad (2)$$

where θ is the angle of the asperity (Figure 6). For each simulation, the y-components acting on the asperities are calculated at the end of shearing (i.e., δ_H = $29D_{50}$).

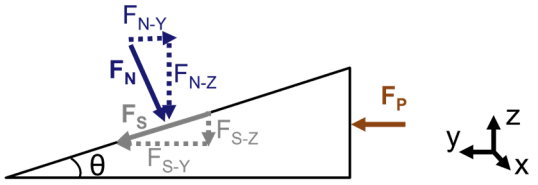

Figure 6. Schematic of the force components acting on the snakeskin-inspired asperities. FN: normal force, FS: sliding force, and FP: passive force.

Each force component is calculated as the sum of all particle-surface contacts of that component type, as shown in Equation (3), where x is the number of particle-wall contacts of one component type on one asperity, i is the asperity-particle contact, and F_n is the particle-wall contact force of component n (where n indicates P, N-Y, or S-Y.)

$$F_C = \sum_{i=0}^{x} F_{n,i} \quad (3)$$

This investigation considers the average forces (F_{avg}) and total force (F_{tot}) components. The average force component provides information on the magnitude of load transfer mobilized at the individual asperity level, and is calculated by summing the force components across all asperities and divided by the number of asperities (N), as follows:

$$F_{avg} = \sum_{j=0}^{N} F_C \ / \ N \quad (4)$$

where j is the current asperity. The total force is directly related to the interface shear strength and accounts for the number of asperities in a given surface. It is calculated as the sum of the force components acting across all asperities, as follows:

$$F_{tot} = \sum_{j=0}^{N} F_C \quad (5)$$

Average and total force components acting on asperities after cranial and caudal shear are shown by Figure 7 and Figure 8 respectively. The figures shed light on the relative contribution of the force components to the mobilization of interface strength and reveal key differences with how shear resistance is mobilized between the cranial and caudal directions.

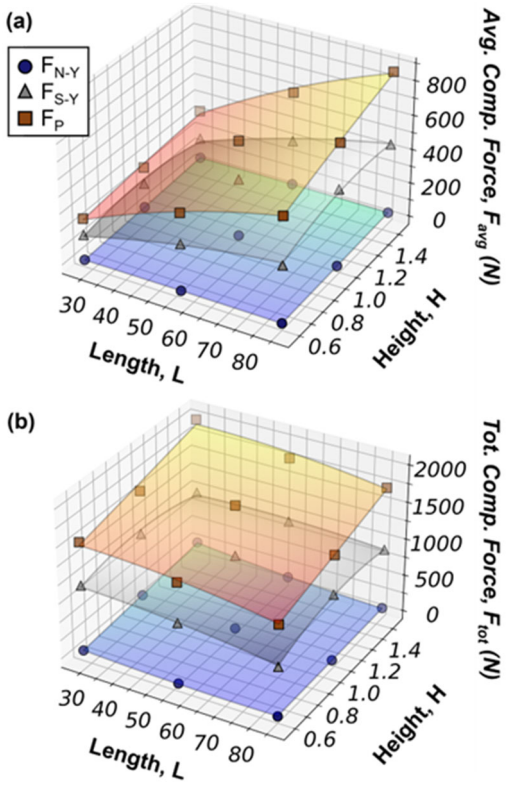

Figure 7. (a) Average and (b) total y-component forces at the end of shearing as a function of L and H for cranial shear.

For cranial shear, the average F_P magnitude was the greatest of all three components for all H and L values, followed by F_{S-Y} and F_{N-Y}, respectively. This is qualitatively consistent with the contact force distributions (Figure 4), where strong force chains formed at the edges of asperities. The F_P component mobilized in cranial shear was similar to the passive component mobilized by surfaces with a structured roughness form, as reported by Hryciw and Irsyam (1993), Frost and DeJong (2005), and Martinez and Frost (2017). The average forces acting on the asperities depended on the H and L. During cranial shear, the magnitude of average F_P and F_{S-Y} components increase with H due to the increase in bearing area and increase with L due to the reduction in interaction between the asperities, as previously shown qualitatively in the comparison Figure 4c and 4d. In contrast, the F_{N-Y} component has a small magnitude in all cases. The total F_P component increases with H due to the increase in bearing area. However, increasing L results in a decrease to the total F_P component. This is because while a higher magnitude of shear resistance is mobilized per asperity as L is increased, the number of asperities increases as L is decreased. The influence of the number of asperities governs, such that the total F_P component and thus the overall shear strength increases as L decreases. The total F_{S-Y} and F_{N-Y} force components are largely independent of L and H.

During caudal shear, F_P was close to zero, indicating that only small active forces are mobilized. In this case, F_{S-Y} contributed the most to overall shear resistance. The average F_{S-Y} and F_{N-Y} components increased with both H and L. Increases to H resulted in steeper asperity slopes, and while increases to L reduced slope, it directly increased the area over which these force components act upon, increasing the number of contact forces over the surface of the asperity. In the case of total force components, while increases to H and decreases to L increases both F_{S-Y} and F_{N-Y} components, this effect was minor. Unlike the total F_P component for cranial shear, the F_{S-Y} and F_{N-Y} components were less influenced by the number of asperities and depended more on the total surface area of the shear surface and the slope of the asperities. L and H affect asperity slope but have little impact on surface area, which is primarily controlled by the specimen size.

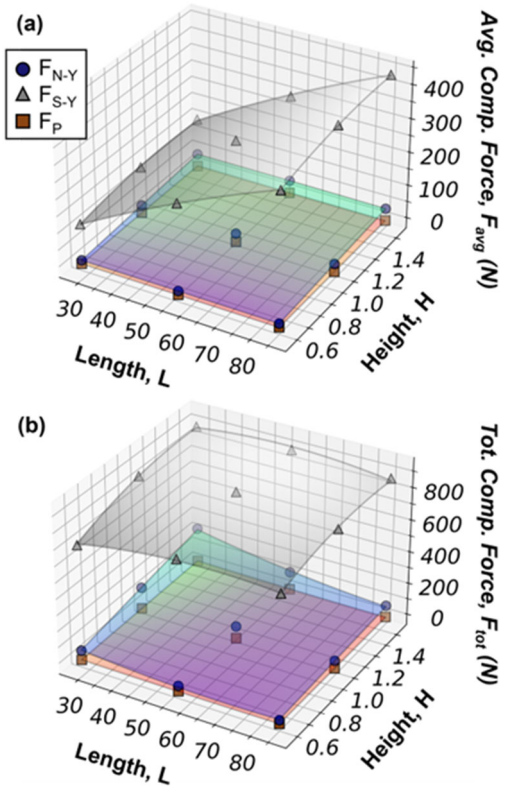

Figure 8. (a) Average and (b) total y-component forces at the end of shearing as a function of L and H for caudal shear.

The F_{S-Y} and F_{N-Y} magnitudes were similar in magnitude in the cranial and caudal shearing directions, as shown by comparison of Figure 7 and Figure 8. Thus, it can be concluded that the F_P component is primarily responsible for the frictional directionality mobilized by the snakeskin-inspired surfaces. Furthermore, changes to asperity geometry influences the F_P component more significantly than the F_{S-Y} and F_{N-Y} components. Since the F_P component is close to zero for caudal shear, this further explains the smaller effect of asperity geometry in this shear direction compared to cranial shear.

6 CONCLUSIONS

Surfaces comprised of asperities inspired by ventral snake scales mobilize frictional directionality. DEM was used to investigate the mechanisms governing the frictional directionality and assess the effects of asperity geometry and shear direction on the interface shear behavior. Cranial shear mobilized higher shear resistance than caudal shear. During cranial shear, strong contact forces mobilized at asperity vertical sides, making up a passive force component. This passive component was absent from caudal shear, where only sliding and normal forces were mobilized over asperities. As such, frictional directionality was attributed primarily to the passive force component. Increases to asperity height resulted in strong increases to cranial passive forces and mild increases to sliding and normal forces. As asperity length increased, the average cranial passive and sliding forces per asperity increased due to reduced interactions between neighboring asperities and increased surface areas, respectively. However, because smaller asperity lengths accommodate more asperities, the total passive component decreases with increasing length.

From this investigation, a clear distinction between different shear behavior types emerges depending on the geometry of the shear surface. Cranial shear with surface geometries with many, closely spaced asperities mobilize a behavior that is similar to that exhibited by a fully rough surface. This shear behavior is characterized by a strain-softening response, high dilatancy, a uniform shear zone at the interface, and uniformly distributed force chains. Cranial shear with sufficiently spaced asperities is dominated by passive resistances, in which contact forces and particle displacements are localized near the vertical sides of asperities. The magnitude of forces mobilized by each individual asperity is greater in this case, but the overall shear strength decreases as fewer asperities fit within the same surface length. Smooth surfaces and caudally sheared snakeskin-inspired surfaces mobilized primarily sliding type behaviors, where shear resistance resulted primarily from the sliding friction between particles and the surface. However, caudally sheared snakeskin-inspired surfaces featured sloped surfaces that resulted in greater amounts of particle displacements and concentrated force chains over asperity surfaces in comparison to smooth surfaces. The findings presented in this paper provide important implications for interface shear behavior across different surface textures and highlight the need for further investigation on how asperity geometry drives behavioral transitions.

7 ACKNOWLEDGEMENTS

This material is based upon work supported by the National Science Foundation (NSF) under Award No. 1942369 and No. EEC–1449501. Any opinions, findings, and conclusions or recommendations expressed in this material are those of the author(s) and do not necessarily reflect those of the NSF.

8 REFERENCES

Blair, B., 2024. *Monotonic and cyclic resistance of MICP cemented silica and carbonate sands*. M.S. thesis. University of California Davis.

DeJong, J.T. and Westgate, Z.J., 2009. Role of initial state, material properties, and confinement condition on local and global soil-structure interface behavior. Journal of Geotechnical and Geoenvironmental Engineering, 135(11), pp.1646–1660.

Dietz, M.S. and Lings, M.L., 2006. Postpeak strength of interfaces in a stress-dilatancy framework. *Journal of Geotechnical and Geoenvironmental Engineering*, 132(11), pp.1474–1484.

Frost, J.D. and DeJong, J.T., 2005. In situ assessment of role of surface roughness on interface response. *Journal of Geotechnical and Geoenvironmental Engineering*, 131(4), pp.498–511.

Gayathri, V.L. and Vangla, P., 2024. Shear behaviour of snakeskin-inspired ribs and soil interfaces. *Acta Geotechnica*, 19(3), pp.1397–1419.

Hryciw, R.D. and Irsyam, M., 1993. Behavior of sand particles around rigid ribbed inclusions during shear. *Soils and Foundations*, 33(3), pp.1–13.

Hu, D.L., Nirody, J., Scott, T. and Shelley, M.J., 2009. The mechanics of slithering locomotion. *Proceedings of the National Academy of Sciences*, 106(25), pp.10081–10085.

Jayne, B.C., 1986. Kinematics of terrestrial snake locomotion. *Copeia*, 1986(4), pp.915–927.

Jing, X.Y., Zhou, W.H., Zhu, H.X., Yin, Z.Y. and Li, Y., 2018. Analysis of soil-structural interface behavior using three-dimensional DEM simulations. *International Journal for Numerical and Analytical Methods in Geomechanics*, 42(2), pp.339–357.

Kulhawy, F.H., 1991. Drilled shaft foundations. In: H.Y. Fang, ed. *Foundation engineering handbook*. Boston, MA: Springer US, pp.537–552.

Lee, S.H., Nawaz, M.N. and Chong, S.H., 2023. Estimation of interface frictional anisotropy between sand and snakeskin-inspired surfaces. *Scientific Reports*, 13(1), p.3975.

Lings, M.L. and Dietz, M.S., 2005. The peak strength of sand-steel interfaces and the role of dilation. *Soils and Foundations*, 45(6), pp.1–14.

Martinez, A. and Frost, J., 2017. The influence of surface roughness form on the strength of sand–structure interfaces. *Géotechnique Letters*, 7, pp.1–8.

Martinez, A., Palumbo, S. and Todd, B.D., 2019. Bioinspiration for anisotropic load transfer at soil–structure interfaces. *Journal of Geotechnical and Geoenvironmental Engineering*, 145(10), p.04019074.

Martinez, A., DeJong, J.T., Akin, I., et al. 2022. Bio-inspired geotechnical engineering: principles, current work, opportunities and challenges. *Geotechnique*, 72(8).

Nguyen, D., Chen, Y. and Martinez, A. 2025. A DEM sensitivity study on the effects of contact parameters on triaxial response for the development of a calibration method. *Computers and Geotechnics*, 184.

O'Hara, K. and Martinez, A., 2020. Monotonic and cyclic frictional resistance directionality in snakeskin-inspired surfaces and piles. *Journal of Geotechnical and Geoenvironmental Engineering*, 146(11), p.04020116.

O'Hara, K. and Martinez, A. 2024. Direction-dependent failure envelopes of sand-structure interfaces with snakeskin-inspired surfaces. *Canadian Geotechnical Journal*, 61(12), pp.1-19.

Sturm, H., 2017. Design aspects of suction caissons for offshore wind turbine foundations. In: *Proceedings of the 19th International Conference on Soil Mechanics and Geotechnical Engineering*.

Uesugi, M. and Kishida, H., 1986. Frictional resistance at yield between dry sand and mild steel. *Soils and Foundations*, 26(4), pp.139–149.

Wang, D., Nejadsadeghi, N., Li, Y., Shekhar, S., Misra, A. and Dijksman, J.A., 2021. Rotational diffusion and rotational correlations in frictional amorphous disk packings under shear. *Soft Matter*, 17(34), pp.7844–7852.

Wang, J., Dove, J.E. and Gutierrez, M.S., 2007. Anisotropy-based failure criterion for interphase systems. *Journal of Geotechnical and Geoenvironmental Engineering*, 133(5), pp.599–608.

Xiao, Y., Cui, H., Shi, J., Qiao, W. and Stuedlein, A.W., 2024. Shear response of calcareous sand-steel snake skin-inspired interfaces. *Acta Geotechnica*, 19(3), pp.1517–1527.

Zhao, C.F. and Kruyt, N.P., 2021. Particle and continuum rotations of granular materials: Discrete-element method simulations and experiment. *Journal of Engineering Mechanics*, 147(11), p.04021090.

Zhang, N. and Evans, T.M., 2018. Three dimensional discrete element method simulations of interface shear. *Soils and Foundations*, 58(4), pp.941–956.

Zhong, W., Liu, H., Wang, Q., Zhang, W., Yongqin, L., Ding, X. and Chen, L., 2021. Investigation of the penetration characteristics of snake skin-inspired pile using DEM. *Acta Geotechnica*, 16, pp.1–17.